

Abundances of disk and bulge giants from high-resolution optical spectra[★]

IV. Zr, La, Ce, Eu

R. Forsberg¹, H. Jönsson^{1,2}, N. Ryde^{1,3}, and F. Matteucci^{4,5,6}

¹ Lund Observatory, Department of Astronomy and Theoretical Physics, Lund University, Box 43, SE-221 00 Lund, Sweden
e-mail: rebecca@astro.lu.se

² Materials Science and Applied Mathematics, Malmö University, SE-205 06 Malmö, Sweden

³ Université Côte d'Azur, Observatoire de la Côte d'Azur, CNRS, Laboratoire Lagrange, Bd de l'Observatoire, CS 34229, 06304 Nice Cedex 4, France

⁴ Dipartimento di Fisica, Sezione di Astronomia, Università di Trieste, via G.B. Tiepolo 11, I-34131, Trieste, Italy

⁵ I.N.A.F. Osservatorio Astronomico di Trieste, via G.B. Tiepolo 11, I-34131, Trieste, Italy

⁶ I.N.F.N. Sezione di Trieste, via Valerio 2, 34134 Trieste, Italy

Received July 18, 2019; accepted September 18, 2019

ABSTRACT

Context. Observations of the Galactic bulge point at a formation through secular evolution of the disk instead of gas dissipation and/or mergers, as previously believed. This would imply very similar chemistry in the disk and bulge. Some elements, like the α -elements are well studied in the bulge, but others, like the neutron-capture elements, are much less well explored. Stellar mass and metallicity are factors that affect the neutron-capture process. Due to this, the enrichment of the ISM and the abundance of neutron-capture elements vary with time, making them suitable probes for the Galactic chemical evolution.

Aims. In this work we make a differential comparison of neutron-capture element abundances determined in the local disk(s) and the bulge, focusing on minimising possible systematic effects in the analysis, with the aim of finding possible differences/similarities between the populations.

Methods. Abundances are determined for Zr, La, Ce and Eu in 45 bulge giants and 291 local disk giants, from high-resolution optical spectra. The abundances are determined by fitting synthetic spectra using the SME-code. The disk sample is separated into thin and thick disk components using a combination of abundances and kinematics.

Results. We find flat Zr, La, Ce trends in the bulge, with a ~ 0.1 dex higher La abundance compared with the disk, possibly indicating a higher s-process contribution for La in the bulge. [Eu/Fe] decreases with increasing [Fe/H], with a plateau at around [Fe/H] ~ -0.4 , pointing at similar enrichment as α -elements in all populations.

Conclusions. We find that the r-process dominated the neutron-capture production at early times both in the disks and bulge. [La/Eu] for the bulge are systematically higher than the thick disk, pointing to either a) a different amount of SN II or b) a different contribution of the s-process in the two populations. Considering [(La+Ce)/Zr], the bulge and the thick disk follow each other closely, suggesting a similar ratio of high/low mass asymptotic giant branch-stars.

Key words. Galaxy: solar neighbourhood, bulge, evolution – Stars: abundances

1. Introduction

Our view of the structure and formation of the Galactic bulge has changed dramatically over the past decade. Earlier, the prevailing view was that the bulge is a spheroid in a disk, formed in an early, rapid, dissipative collapse (e.g. Immeli et al. 2004), naturally resulting from, for instance, major mergers converting disks to classical bulges (e.g. Shen & Li 2016). However, with

new findings and data accumulating, what we call the bulge is today predominately considered to be mainly the inner structures of the Galactic bar seen edge-on (e.g. Portail et al. 2017). The details of its structure and timescales for its formation is, however, not clear (e.g. Barbuy et al. 2018).

Metallicity distributions and abundance-ratio trends with metallicity provide important means to determine the evolution of stellar populations, also in the bulge. Trends of different element groups formed in different nucleosynthetic channels provide strong complementary constraints. Also, comparisons of trends between different stellar populations, e.g. the local thick disk, can constrain the history of the bulge. Whether or not there is an actual difference in abundance trends with metallicity between the bulge and the local thick disk is not clear (McWilliam 2016; Barbuy et al. 2018; Zasowski et al. 2019; Lomaeva et al. 2019). Some elements such as Sc, V, Cr, Co, Ni and Cu show differences in some investigations, whereas others show great

[★] Based on observations made with the Nordic Optical Telescope (programs 51-018 and 53-002), operated by the Nordic Optical Telescope Scientific Association at the Observatorio del Roque de los Muchachos, La Palma, Spain, of the Instituto de Astrofísica de Canarias, spectral data retrieved from PolarBase at Observatoire Midi Pyrénées, and observations collected at the European Southern Observatory, Chile (ESO programs 71.B-0617(A), 073.B-0074(A), and 085.B-0552(A)). Tables A.1-A.4 are only available in electronic form at the CDS via anonymous ftp to cdsarc.u-strasbg.fr (130.79.128.5) or via <http://cdsweb.u-strasbg.fr/cgi-bin/qcat?J/A+A/>

similarities. New abundance studies minimising systematic uncertainties are clearly needed.

An important nucleosynthetic channel that has not yet been thoroughly investigated in the bulge is that of the heavy elements, namely the neutron-capture elements. These can be divided into two groups: the slow (s)- and rapid (r)-process elements, depending on the timescales between the subsequent β -decay and that of the interacting neutron flux (Burbidge et al. 1957). The neutron flux in the s-process is such that the time scale of interaction is *slower* than the subsequent β -decay, making the elements created in this process to trace the valley of stability, whilst it is the other way around for the r-process, resulting in creation of heavier elements. As a point of reference, the s-process therefore produces the lighter elements after iron ($A \geq 60$), whereas the r-process is the dominating production process for the heaviest elements. Nonetheless, it is important to keep in mind that the production of heavier elements is a combination of the two processes and a “s- or r-process element” simply refers to an element having a dominating contribution from one of the processes. The neutron densities required for the s- and the r-process are $\leq 10^7 - 10^{15} \text{ cm}^{-3}$ (Busso et al. 1999; Karakas & Lattanzio 2014) and somewhere between $10^{24} - 10^{28} \text{ cm}^{-3}$ (Kratz et al. 2007), respectively, putting some constraints on the astrophysical sites where they can occur.

The s-process can in turn be divided into three sub-processes: the *weak*, *main* and *strong* s-process, taking place in massive stars (weak) and asymptotic giant branch (AGB) stars (main, strong). Furthermore, the s-process *elements* can be divided into the light, heavy and very heavy s-process elements, the naming originating from their atomic masses of $A = 90, 138$ and 208 (around Zr, La and Pb, respectively). A build-up is created at these stable nuclei ($N = 50, 82$ and 126 , also known as magic numbers) due to isotopes with low neutron cross sections, creating bottlenecks in the production of heavier elements and in turn, peaks of stable isotopes. Thus, the naming first- second- and third-peak s-process is often used too for the light, heavy and very heavy s-process elements. In this work, light and heavy s-process elements produced in the main s-process will be analysed (Zr, La, Ce).

The main s-process takes place in the interior of low- and intermediate-mass AGB stars (Herwig 2005; Karakas & Lattanzio 2014) with the neutrons originating from the reactions $^{13}\text{C}(\alpha, n)^{16}\text{O}$ and $^{22}\text{Ne}(\alpha, n)^{25}\text{Mg}$. The second reaction takes place at higher temperatures in AGB stars with initial mass of $> 4 M_{\odot}$. The process takes place in the so-called ^{13}C -pocket in-between the hydrogen and helium burning shells during the third dredge-up (TDU; Bisterzo et al. 2017). Since AGB stars have an onset delay on cosmic scales, a non-negligible fraction of the s-process-dominated elements is likely to originate from the r-process at early times. Furthermore, the light s-process elements (first-peak s-process) can have a possible production from the weak s-process, taking place in helium core burning and in the subsequent convective carbon burning shell phase, in massive stars (Couch et al. 1974). However, previous observations can not, to a full extent, explain the abundance of the light s-process elements at early times and other possibilities of their origin have therefore been proposed (e.g. LEPP; Travaglio et al. 2004; Cristallo et al. 2015).

The production site(s) for r-process elements is yet to be constrained, but the proposed sites are various neutron-rich (violent) events, such as core collapse supernovae (CC SNe), collapsars and the mergers of heavy bodies in binaries, like neutron star mergers (Snedden et al. 2000; Thielemann et al. 2011; Thielemann et al. 2017). The electromagnetic counterpart to the ob-

served neutron merger GW170817 (Abbott et al. 2017) indeed showed r-process elements. Research is still ongoing to determine whether or not neutron star mergers is the only, or even the dominating, source of r-process elements (e.g. Thielemann et al. 2018; Côté et al. 2019; Siegel et al. 2019; Kajino et al. 2019).

In order to put constraints on the neutron capture yields, it is important to have reliable observational abundances to compare with the models. In the review paper on the chemical evolution of the bulge by McWilliam (2016), the necessity of having properly measured abundances for the disk in order to have a reference sample for bulge measurements is stressed, which is provided in this work.

Regarding the determination of neutron-capture elements in bulge stars, such analyses have been made previously by Johnson et al. (2012), Van der Swaelmen et al. (2016), and Duong et al. (2019). Johnson et al. (2012) studied stars in Plaut’s field ($b = -8^{\circ}$) observed with the Hydra multifiber spectrograph at the Blanco 4m telescope, determining the abundances of Zr, La, Nd and Eu. Their [La/Fe] trend versus metallicity of the stars in the bulge field is clearly different from that of the thick disk. They thus conclude that the metal-poor bulge, or the inner disk, is likely chemically different from that of the thick disk. Van der Swaelmen et al. (2016) studied Ba, La, Ce, Nd, and Eu in 56 Galactic bulge giants, observed with FLAMES/UVES at the VLT, finding that the s-process elements Ba, La, Ce, Nd, have decreasing [Ba,La,Ce,Nd/Fe] abundances with increasing metallicity, separating them from the flatter thick disk trends. Additionally, in the work by Duong et al. (2019), Zr, La, Ce, Nd, and Eu is measured for a large bulge sample at latitudes of $b = -10^{\circ}, -7.5^{\circ}$ and -5° , observed with the HERMES spectrograph on the Anglo-Australian Telescope. They find indications of the bulge having a higher star formation rate than that of the disk.

Johnson et al. (2012) and Van der Swaelmen et al. (2016) compare their bulge abundances with previously determined disk abundances, mainly from dwarf stars, which might obstruct the interpretation of the comparative abundances due to the risk of systematic uncertainties between analyses of dwarf and giant stars¹. Previous works by Meléndez et al. (2008) and Gonzalez et al. (2015) stressed the importance of comparing stars within the same evolutionary stage. Furthermore, in investigations of atomic diffusion and mixing in stars (Korn et al. 2007; Lind et al. 2008; Nordlander et al. 2012; Gruyters et al. 2016; Souto et al. 2019; Liu et al. 2019), it has been shown that dwarf stars might have systematically lower elemental abundances compared to evolved stars, suggesting that abundances measured from dwarf stars are too low. The magnitude of this depletion is measurable and should, in general, be considered for the relevant elements in order to properly probe the Galactic composition and its evolution based on dwarf stars.

In this paper, we study the four neutron-capture elements Zr, La, Ce, and Eu, determined from optical spectra of giants observed with FLAMES/UVES for the bulge sample. We compare the obtained abundance-ratio trends with that of the local disk, obtained from a comparison sample of similarly analysed giants (observed with FIES at high resolution in the same wavelength range). Section 2 describe the bulge and disk samples. The same methodology for determining the stellar parameters and abundances (a carefully chosen set of spectral lines) ensures a minimisation of the systematic uncertainties in the comparison of the two samples, following the same methodology as the previ-

¹ Duong et al. (2019) do, to a large extent as possible, use the same atomic data and analysis method in their work as their comparison sample, GALAH (Buder et al. 2018), to minimise systematic offsets.

ous papers in this series; Jönsson et al. (2017a,b); Lomaeva et al. (2019), see Sect. 3. We present the results in Sect. 4 and discuss these in Sect. 5.

2. Observations

2.1. Bulge sample

Since large amounts of dust lies in the line-of-sight toward the Galactic centre, resulting in a high optical extinction, observing bulge stars can be challenging at optical wavelengths. Our ambition was to include fields as close to the centre of the bulge as possible, whilst keeping to regions where the extinction is manageable.

The Galactic bulge sample consists of 45 giants (see Table A.1). The spectra were obtained using the spectrometer FLAMES/UVES mounted on the VLT, Chile, observed in May–August 2003–2004. 27 of these spectra were also analysed in Van der Swaelmen et al. (2016). In addition to these, 18 spectra from the Sagittarius Window, $(l, b) = (1.29^\circ, -2.65^\circ)$, lying closer to the Galactic plane in a region with relatively low extinction, is added to the sample analysed here. These were observed in August 2011 (ESO programme 085.B-0552(A)). In total, five bulge fields are included in the bulge sample: SW (the Sagittarius Window), BW (Baade’s Window), BL (the Blanco field), B3 and B6². The fields can be seen in Fig. 1, overlaid on an optical extinction map, together with the fields analysed in Johnson et al. (2012) and Duong et al. (2019). From Fig. 1 one can see that the SW field lies in a region of relatively low extinction and closer to the Galactic plane than the other fields.

The FLAMES/UVES instrument allows for simultaneous observation of up to seven stars. Depending on the extinction, and local conditions, each setting in our observations required an integration time of somewhere between 5–12 hours. The achieved signal-to-noise ratios (S/N) of the recorded bulge spectra are between 10–80. The resolving power of the spectra is $R \sim 47\,000$ and the usable wavelength coverage is limited to the range 5800 and 6800 Å.

The distances to our bulge stars are estimated to range between 4–12 kpc from the Solar System (Bailer-Jones et al. 2018), placing the stars within the Galactic regions classified as the bulge by Wegg et al. (2015). Although it should be noted that distance estimation can be rather troublesome and Gaia DR2 (Gaia Collaboration et al. 2016, 2018) reports a parallax uncertainty higher than 20 % for a majority of our bulge stars.

2.2. Disk sample

The disk sample consists of 291 giants stars, a majority of these placed within 2 kpc from the Solar System (see Table A.2). The bulk of the sample is observed at the Nordic Optical Telescope (NOT), La Palma, using the Fibre-fed Echelle Spectrograph (FIES; Telting et al. (2014)), under the programme 51-018 (150 stars) in May–June 2015 and 53-002 (63 stars) in June 2016. 41 spectra were taken from the stellar sample in Thygesen et al. (2012), also observed using the FIES at the NOT. An additional 18 spectra were downloaded from the FIES archive. Lastly, 19 spectra were taken from the PolarBase data base (Petit et al. 2014) where NARVAL and ESPaDOnS have been used (mounted on Telescope Bernard Lyot and Canada-France-

Hawaii Telescope, respectively). FIES and PolarBase have similar resolving powers of $R \sim 67\,000$ and $R \sim 65\,000$, respectively.

All three spectrometers cover wide regions in the optical domain, but in order to maximise the coherency in this work, the wavelength region used is restricted to that of the bulge spectra; 5800–6800 Å. The resulting S/N of the FIES spectra are around 80–120 per data point in the reduced spectrum. Similar values can be found for the PolarBase spectra whereas the Thygesen et al. (2012) spectra have a lower S/N of about 30–50. Details about how the S/N was calculated can be found in Jönsson et al. (2017a).

The reduction of the FIES spectra was performed using the standard FIES pipeline and the Thygesen et al. (2012) and PolarBase data was already reduced. A crude normalisation of all spectra was done initially with the IRAF task `continuum`. Later in the analysis, the continuum is re-normalised more carefully by a manual placement of continuum regions and subsequently fitting a straight line to these, allowing a higher precision of the abundance determination (more on this in Sect. 3.3).

Telluric lines have not been removed from the spectra, instead, a telluric spectrum from the Arcturus atlas (Hinkle et al. 2000) has been plotted over the appropriately-shifted observed spectra and affected regions have been avoided on a star-by-star basis.

3. Analysis

The analysis of the spectra and the determination of the stellar abundances follows the same methodology as described in the previous papers in this series; Jönsson et al. (2017a,b) and Lomaeva et al. (2019). This section describes the general methodology as well as the specifics relevant for this work.

3.1. General methodology

To determine the stellar abundances synthetic spectra are modelled using the tool Spectroscopy Made Easy (SME, Valenti & Piskunov 1996; Piskunov & Valenti 2017). For a given set of stellar parameters (T_{eff} , $\log g$, $[\text{Fe}/\text{H}]$, and microturbulence, ξ_{micro}), SME interpolates in a grid of pre-calculated model atmospheres and calculates a synthetic spectrum of a region of choice. By defining line and continuum masks over spectral regions of interest, SME can simultaneously fit, using χ^2 -minimisation (Marquardt 1963), both stellar photospheric parameters and/or stellar abundances. Figure 2 shows the line definitions and continuum placements for the bulge star B6-F1 and the spectral lines used in the analysis.

The stellar parameters of the stars analysed are determined as described in Sect. 3.2 below. Metallicity-scaled solar abundances (Grevesse et al. 2007) are assumed in SME, except for the α -elements that have already been determined in Jönsson et al. (2017b).

SME uses a grid of MARCS models³ (Gustafsson et al. 2008) that adopts spherical symmetry for $\log g < 3.5$, which is the case for a majority of our stars, otherwise plane parallel. Some non-local thermodynamic equilibrium (NLTE) effect has been reported for the elements analysed here: Zr is shown by Velichko et al. (2010) to be weakly dependent on temperature; and Mashonkina & Gehren (2000) find that they need small NLTE corrections of the order of +0.03 dex for Eu in their analysis of cool dwarfs. Nonetheless, the analysis in this work is done under the assumption of LTE.

² The naming of the fields follows the convention seen in Lecureur et al. (2007)

³ Available at marcs.astro.uu.se

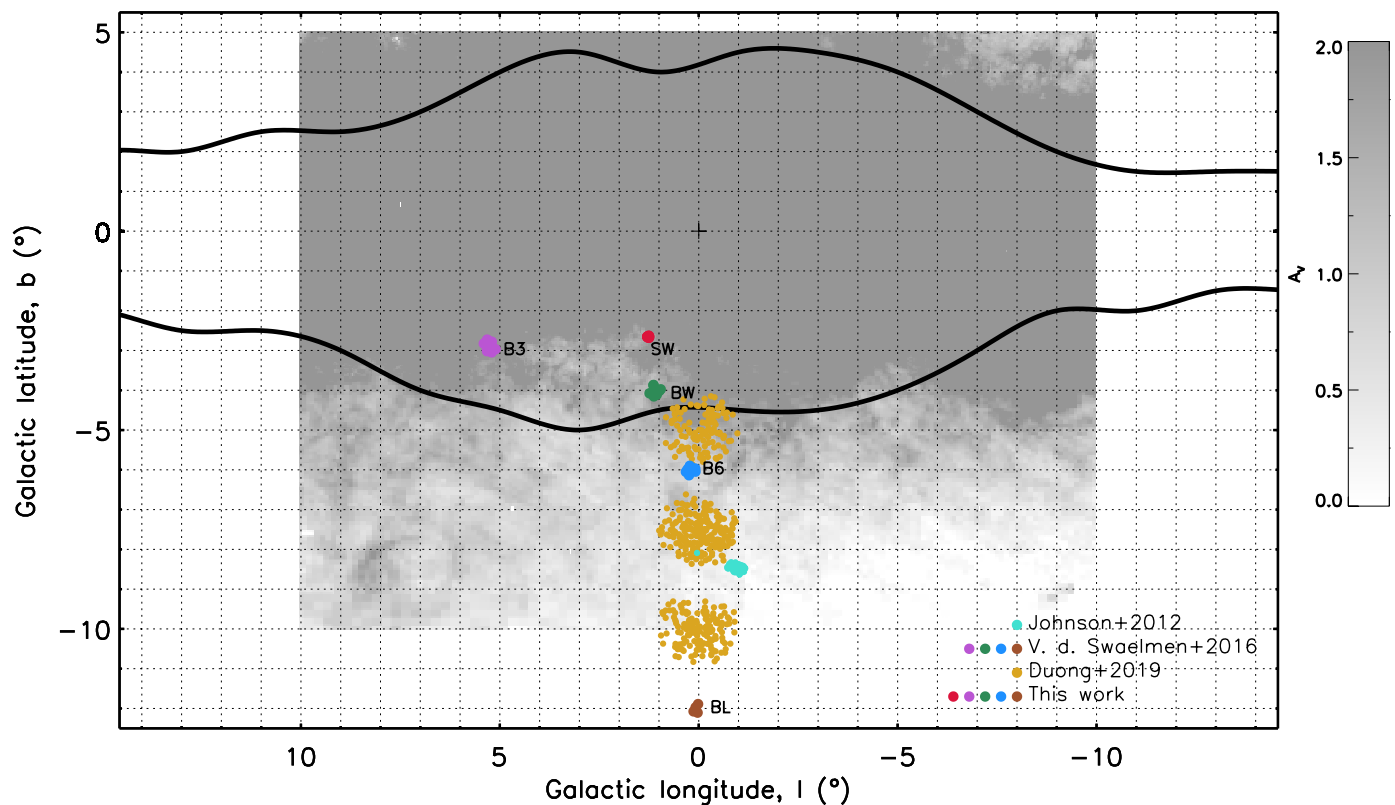


Fig. 1. Map of the Galactic bulge showing the five analysed fields (SW, B3, BW, B6, and BL). The bulge samples from Johnson et al. (2012), Van der Swaelmen et al. (2016) and Duong et al. (2019) are also marked in the figure. The dust extinction towards the bulge is taken from Gonzalez et al. (2011, 2012) scaled to optical extinction (Cardelli et al. 1989). The scale saturates at $A_V = 2$, which is the upper limit in the figure. The COBE/DIRBE contours of the Galactic bulge, in black, are from Weiland et al. (1994).

3.2. Stellar parameters

The stellar parameters used are determined in Jönsson et al. (2017a,b) (where a more detailed description can be found) by fitting synthetic spectra for unsaturated and unblended Fe I and Fe II lines, Ca I lines and $\log g$ sensitive Ca I line wings, while T_{eff} , $\log g$, $[\text{Fe}/\text{H}]$, ξ_{micro} , and $[\text{Ca}/\text{Fe}]$ were set as free parameters in SME. Fe I has NLTE corrections adopted from Lind et al. (2012). The reported uncertainties for these parameters in Jönsson et al. (2017a,b) for a typical disk star of $S/N \sim 100$ are $T_{\text{eff}} \pm 50$ K, $\log g \pm 0.15$ dex, $[\text{Fe}/\text{H}] \pm 0.05$ dex and ± 0.1 km/s for ξ_{micro} . For a typical bulge star, the S/N is significantly lower (median of 38), and hence the uncertainties greater; $T_{\text{eff}} \pm 100$ K, $\log g \pm 0.30$ dex, $[\text{Fe}/\text{H}] \pm 0.10$ dex and $\xi_{\text{micro}} \pm 0.2$ km s $^{-1}$. These values are later used in the uncertainties estimations, see Sect. 4.1.

3.3. Abundance determination

The atomic line data used for the abundance determination are collected from the *Gaia*-ESO line list version 6 (Heiter et al. 2015, Heiter et al., in prep.). From here we get wavelengths, excitation energies and transition probabilities (as well as broadening parameters, when existing). The transition probabilities for the elements investigated here, Zr, La, Ce, and Eu, come from Biemont et al. (1981), Lawler et al. (2001a), Lawler et al. (2009),

and Lawler et al. (2001b), respectively. All available lines for these elements in the given wavelength region (5800-6800 Å) were investigated individually in order to exclude lines that could not be modelled properly (due to blends, bad atomic data or other systematics). As for Zr, where three separate lines were suitable for abundance determination, the lines were ultimately fitted simultaneously. Finally, the determined SME abundances were, in the post-process, re-normalised to the most up-to-date solar values provided by Grevesse et al. (2015). The final set of lines used for abundance determination is presented in Table 1. Apart from the atomic lines, we include the molecules C_2 (Brooke et al. 2013) and CN (Snedden et al. 2014) in the synthesis.

For La and Eu hyperfine splitting (hfs) had to be taken into account. By not taking hfs into account there is a risk of overestimating the measured abundance (Prochaska & McWilliam 2000; Thorsbro et al. 2018). Additionally, isotopic shift (IS) has to be considered for Zr, Ce and Eu. The shift is caused by the isotopes having shifted energy levels, resulting in radiative transitions with shifted wavelengths. IS is included by manually identifying the set of transitions for each isotope in the line list and scaling the $\log(gf)$ to the relative solar isotopic abundances, see Table 2.

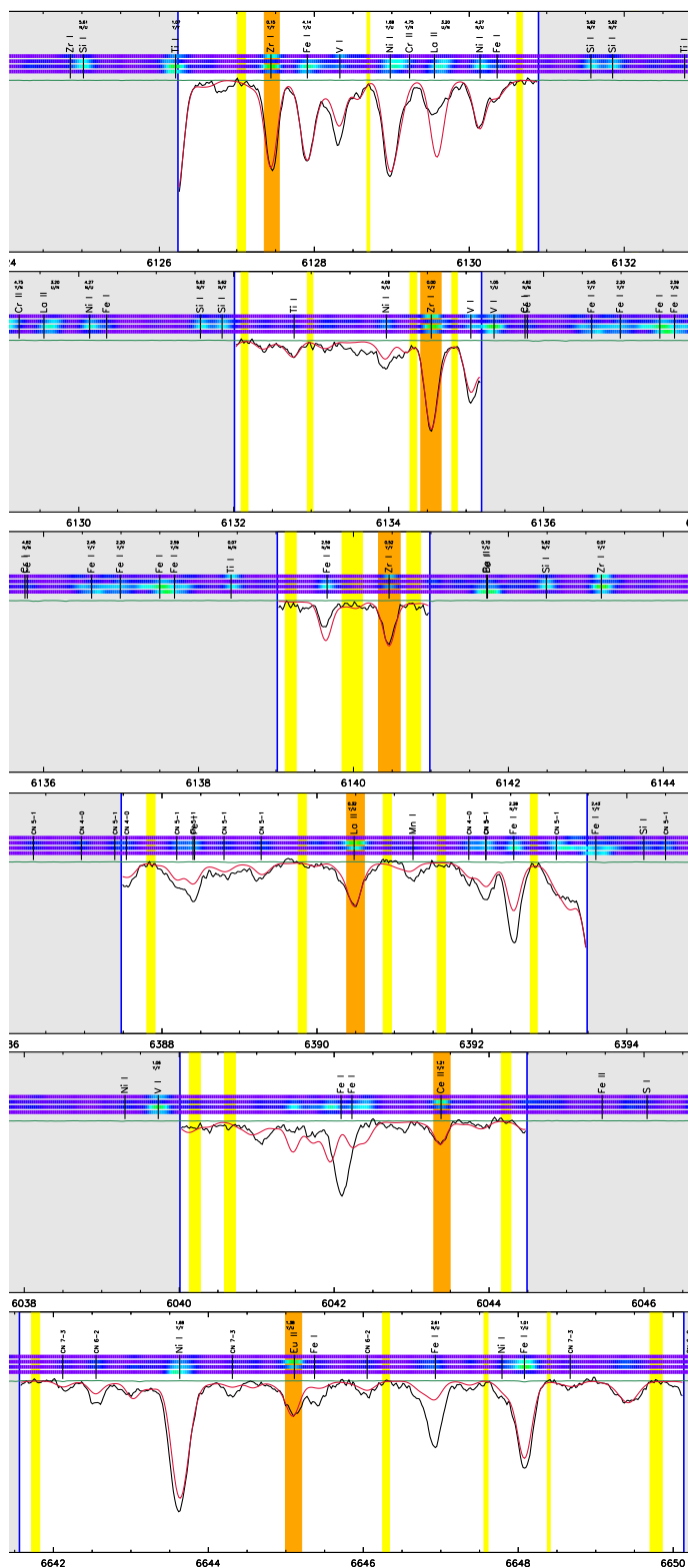


Fig. 2. The observed spectrum (black) of the bulge star B6-F1 ($S/N = 54$). The lines for abundance determination of Zr (three lines), La, Ce and Eu (one line each) are marked out as the orange regions. The yellow regions are the manually placed continuum and the red spectrum is the synthetic one. The segments within which the synthetic spectrum is modelled are marked as the white wavelength regions between the blue vertical lines in each panel. The four horizontal lines above each spectrum indicates the lines' sensitivity in the stellar parameters T_{eff} , $\log g$, $[\text{Fe}/\text{H}]$ and ξ_{micro} , respectively, where green is more sensitive than blue.

Table 1. Atomic lines used in the analysis. The elements and ionisation stages are given in Col. 1, the transition wavelengths in Col. 2, and the $\log(gf)$ values are listed in Col. 3. The excitation energies of the transitions lower level are given in Col. 4. The $\log(gf)$ data included in the Gaia-ESO line lists comes from Biemont et al. (1981) (Zr), Lawler et al. (2001a) (La), Lawler et al. (2009) (Ce) and Lawler et al. (2001b) (Eu).

Element	Wavelength [\AA]	$\log(gf)$	$\chi_{\text{exc}}^{\text{low}}$ [eV]
Zr I	6127.440	-1.06	0.15
Zr I	6134.550	-1.28	0.00
Zr I	6140.460	-1.41	0.51
La II	6390.457	-2.01	0.32
La II	6390.469	-2.08	0.32
La II	6390.486	-1.90	0.32
La II	6390.501	-2.08	0.32
Ce II	6043.373	-0.48	1.21
Eu II	6645.057	-0.84	1.38
Eu II	6645.060	-0.78	1.38
Eu II	6645.068	-2.13	1.38
Eu II	6645.074	-0.84	1.38
Eu II	6645.083	-0.91	1.38
Eu II	6645.086	-0.90	1.38
Eu II	6645.098	-0.60	1.38
Eu II	6645.101	-0.95	1.38
Eu II	6645.121	-1.01	1.38
Eu II	6645.137	-1.09	1.38
Eu II	6645.149	-1.19	1.38

3.4. Population separation

The classification of the stellar populations in the disk (thin/thick) can be done in several ways, by kinematics, age, geometry and chemistry. Even so, the separation of these two components is somewhat debated and the transition between them might be a gradient rather than a clear separation. The results by Hayden et al. (2015) show that the scale length of the thin disk extends further out than that of the thick disk. The thick disk has been shown to be enriched in α -elements, compared to that of the thin disk, in addition to thick disk stars having higher total velocities whilst slower rotational velocities (Bensby et al. 2014).

In Lomaeva et al. (2019) the separation into the two populations is computed for our disk sample, using a combination of stellar metallicity, abundances ($[\text{Ti}/\text{Fe}]$ as determined in Jönsson et al. (2017b)) and kinematics. The radial velocities from Table A.2, proper motions from Gaia DR2 Gaia Collaboration et al. (2016, 2018) and distances from McMillan (2018) are used to calculate the total velocities⁴. In total, kinematic data were available for 268 stars in the disk sample. The clustering method Gaussian Mixture Model (GMM), obtained from the scikit-learn module for Python (Pedregosa et al. 2011), is used to cluster the disk data into the two components. The reader is referred to Lomaeva et al. (2019) for more details.

4. Results

Our derived abundance ratios, $[\text{X}/\text{Fe}]$, for Zr, La, Ce, and Eu, are plotted against $[\text{Fe}/\text{H}]$ in Fig. 3. The population separation is applied to the disk sample and the number of stars in each population for which we could determine the abundance in question is noted in every panel. The bulge sample is plotted on top of the

⁴ $V_{\text{tot}}^2 = U^2 + V^2 + W^2$

Table 2. Isotope information of the elements. Col. 2 gives the baryon number of the stable isotopes that contribute to at least 1 % to the solar system abundance. Col. 3 gives the corresponding relative isotopic abundances of the stable isotopes as measured in the Sun, with references in the last column.

Element(Z)	Baryon number	Relative abundance	Reference
Zr(40)	90:91:92:94:96	51:11:17:17:3	Nomura et al. (1983)
La(57)	139	100	de Laeter & Bukilic (2005)
Ce(58)	140:142	88:11	Chang et al. (1995)
Eu(63)	151:153	48:52	Chang et al. (1994)

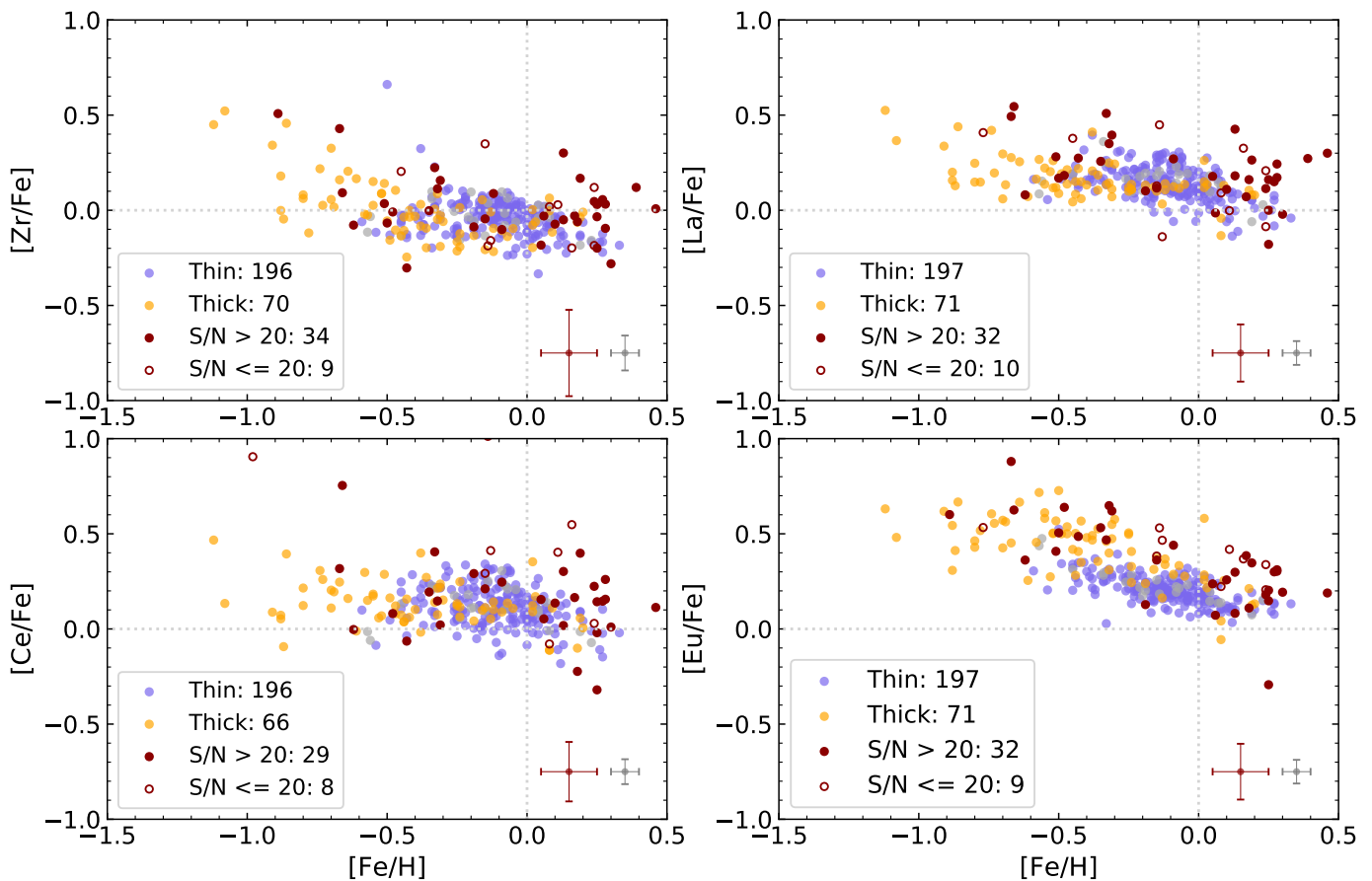


Fig. 3. The abundance ratio trends with metallicity, $[X/Fe]$ against $[Fe/H]$, for the thin- (blue) and thick-disk (yellow) stars as well as the bulge stars (red). Since not all abundances were possible to determine in all spectra, the number of stars in each sample is included in the legend. Filled dark red indicate bulge stars with a S/N above 20, whereas the hollow red circles indicate a S/N equal to or less than 20. Some of the disk stars could not be classified as thick or thin disk stars; these are marked as grey dots. The typical uncertainty for the disk and the bulge sample, as described in Sect. 4.1, is marked in the lower right corner of every plot.

disk trends, differentiating between spectra of higher or lower S/N-ratio of 20. The typical uncertainty is noted in the plots, where the estimation of these is described in Sect. 4.1.

4.1. Uncertainties

Systematic errors generally originate from incorrectly determined stellar parameters, model atmosphere assumptions, continuum placement and atomic data. This makes these errors hard to estimate. To get a sense of the systematic uncertainties, one can compare to reference stars. In Jönsson et al. (2017a) they compare the determined stellar parameters to those of three overlapping Gaia benchmark stars determined in Jofré et al. (2015) and find that these are within the uncertainties of the Gaia benchmark parameters.

All spectra are analysed using the same line and continuum masks as well as the same atomic data, minimising possible random uncertainties. Therefore, the random uncertainties are to primarily be found in the (random) uncertainties of the stellar parameters. An approach to estimate the random uncertainties due to changes in the stellar parameters, is to analyse a typical spectrum several times using parameters that all vary within given distributions. The same method for estimating the uncertainties was used in Lomaeva et al. (2019).

Hence, using the FIES spectrum of the standard star Arcturus⁵, uncertainties were added to its initial stellar parameters, meaning that the stellar parameters were changed simultaneously, for a set of 500 runs with modified stellar parameters. A

⁵ The giant star Arcturus (also known as α -Boo or HIP69673) has been analysed extensively due to its brightness, being the fourth brightest in the night sky, and is suitable as a reference of a typical giant star.

Table 3. The estimated typical uncertainties for the disk and bulge sample using a generated set of stellar parameters for the giant star α -Boo.

$\sigma A_{\text{parameters}}$	Zr	La	Ce	Eu
disk [dex]	0.09	0.06	0.07	0.06
bulge [dex]	0.23	0.15	0.16	0.15

Gaussian distribution is used to generate the uncertainties, using the reported stellar parameter uncertainties as standard deviation (see Sect. 3.2). In the uncertainty estimation of the bulge abundances, we have not degraded the FIES Arcturus spectrum (with a resolution of 67000) to match that of the bulge spectra (R of 47000), but separate tests have shown this slightly lower resolution to have a negligible effect on the determined abundance.

The abundance uncertainties coming from the uncertainties in the stellar parameters are then calculated as

$$\sigma A_{\text{parameters}} = \sqrt{|\delta A_{T_{\text{eff}}}|^2 + |\delta A_{\log g}|^2 + |\delta A_{[\text{Fe}/\text{H}]}|^2 + |\delta A_{v_{\text{micro}}}|^2}, \quad (1)$$

where, for non-symmetrical abundance changes, the mean value is used in the squared sums. The resulting uncertainties can be seen in Table 3.

5. Discussion

In this section we elaborate on the results. First, we compare separately our abundance trends for the disks and bulge with previous literature studies in Sect. 5.1. Second, and this is the core of this investigation, in Sect. 5.2 we consider a more in-depth comparative analysis between our abundances for the bulge and disks populations, both determined in the same way. This is done to minimise the systematic uncertainties as much as possible. We then proceed in considering and discussing comparative abundance ratios such as [Eu/Mg], [Eu/La] and [second-peak s /first-peak s], also in Sect. 5.2 as well as 5.3.

To highlight features of the trend-plots, the running mean of the samples are calculated and plotted (with a 1σ scatter). The number of data points in the running window are set to roughly 15 % of the sample sizes (thin disk, thick disk, bulge). As a result, the running mean (and scatter) does not cover the whole trend range. For the bulge sample, only data points with $S/N > 20$ are included in the running mean. From here and henceforth, the running mean-trend is the one referred to when describing [X/Fe] or [X/Y] ratios (except for Sect. 5.1.1).

5.1. Comparison with selected literature trends

5.1.1. Disk sample

In Fig. 4 we compare our determined disk abundances with those determined for dwarf stars in the disk by Battistini & Bensby (2016). In general, the trends are similar for all elements, as well as the scatter in the determined abundance. The abundances of [La,Ce,Eu/Fe] seem to be systematically higher than those of Battistini & Bensby (2016) whereas the [Zr/Fe]-abundances seem a bit lower. The typical abundance uncertainties for Battistini & Bensby (2016) are 0.12, 0.11, 0.12 and 0.08 dex for Zr, La, Ce and Eu, respectively (their Table 6), which is somewhat higher than ours (see Table 3). The possible shifts in the abundances could be due to systematic differences in dwarf and giant stars or in differing atomic data such as using different lines in the abundance determination. Indeed, there is no overlap in the atomic lines used in these two data sets, except for the La line

at 6390 Å, although Battistini & Bensby (2016) uses three additional lines for the La abundance determination.

Zr is a first-peak s -process element whereas La and Ce are second-peak s -process elements. [Zr,La/Fe] have somewhat decreasing abundances with increasing metallicities, with a flattening of abundances for [Fe/H] above ~ -0.4 . The [Ce/Fe] trend is flatter than [Zr/Fe] and [La/Fe], explained by the higher s -process contribution in the Ce production (66 %, 76 % and 84 % s -process contribution for Zr, La and Ce, respectively (Bisterzo et al. 2014)).

The scatter for the [La/Fe] abundances is higher, ~ 0.5 dex, over the metallicity range [-0.2, 0], compared to the rest of the metallicity domain with ~ 0.3 dex. It indicates AGB stars producing the bulk of s -elements through the main s -process. The increase in scatter can most likely be explained by the mass range of AGB stars, which 1) enables stars to produce s -process elements at different metallicities (times) as well as 2) different amounts of production of the first-/second-peak s -process for different mass AGB stars (see Sect. 5.3). The increasing abundances when [Fe/H] is below -0.5 for the s -process elements Zr and La point at a production by the r -process at early times (see [Eu/Fe]). In addition to Battistini & Bensby (2016), our work compares with the abundances reported in Mishenina et al. (2013) (Zr, La, Ce, Eu) and Delgado Mena et al. (2017) (Zr, Ce, Eu), on dwarf stars in the local disk, see Fig. 5. The typical uncertainties from Mishenina et al. (2013) and Delgado Mena et al. (2017) are chosen from their estimates of low T_{eff} stars, their table 3 and table 4, respectively.

For Eu, the trend decreases with increasing metallicities throughout our metallicity range, except for a plateau around [Fe/H] < -0.6 . Eu has a reported r -process contribution of 94 % (Bisterzo et al. 2014) and the observed trend indicates that the r -process has a continuous enrichment in the Galaxy, similar to that of the α -elements. Our Eu abundances compare well with those of Guiglion et al. (2018), including some subgiant and giant stars in their sample, see Fig. 5. We note that our measurements, Battistini & Bensby (2016) and Guiglion et al. (2018) show slightly, on average, supersolar [Eu/Fe] abundances at solar metallicities, which is not seen in either Mishenina et al. (2013) nor Delgado Mena et al. (2017). Of all the trends, ours is most systematically high not passing through the solar value at any metallicities.

5.1.2. Bulge sample

In Fig. 6 we compare our bulge trend with those observed in Johnson et al. (2012), Van der Swaelmen et al. (2016) and Duong et al. (2019). As for Van der Swaelmen et al. (2016), 27 of the stars/spectra overlap with their work and the same spectral lines are used for the abundance determination. Nonetheless, we observe different trends as well as measure Zr in these stars.

Zirconium: In general, our [Zr/Fe] trend with metallicity is flat, with an increase at lower metallicities [Fe/H] < -0.5 . It should be noted that the running mean is rather poorly defined at the edges and the feature is based primarily on the two most metal-poor stars in Fig. 3. Our trend agrees well with that of Johnson et al. (2012) within our overlapping metallicity ranges, whereas Duong et al. (2019) has overall decreasing abundances with increasing metallicities. Above [Fe/H] ~ 0.1 , our [Zr/Fe] is solar while Johnson et al. (2012) and Duong et al. (2019) have subsolar [Zr/Fe], ours pointing at a higher s -process contribution in the production of Zr.

Lanthanum: Johnson et al. (2012) reports a dip in [La/Fe] abundance around [Fe/H] ~ -0.4 which is not observed in either

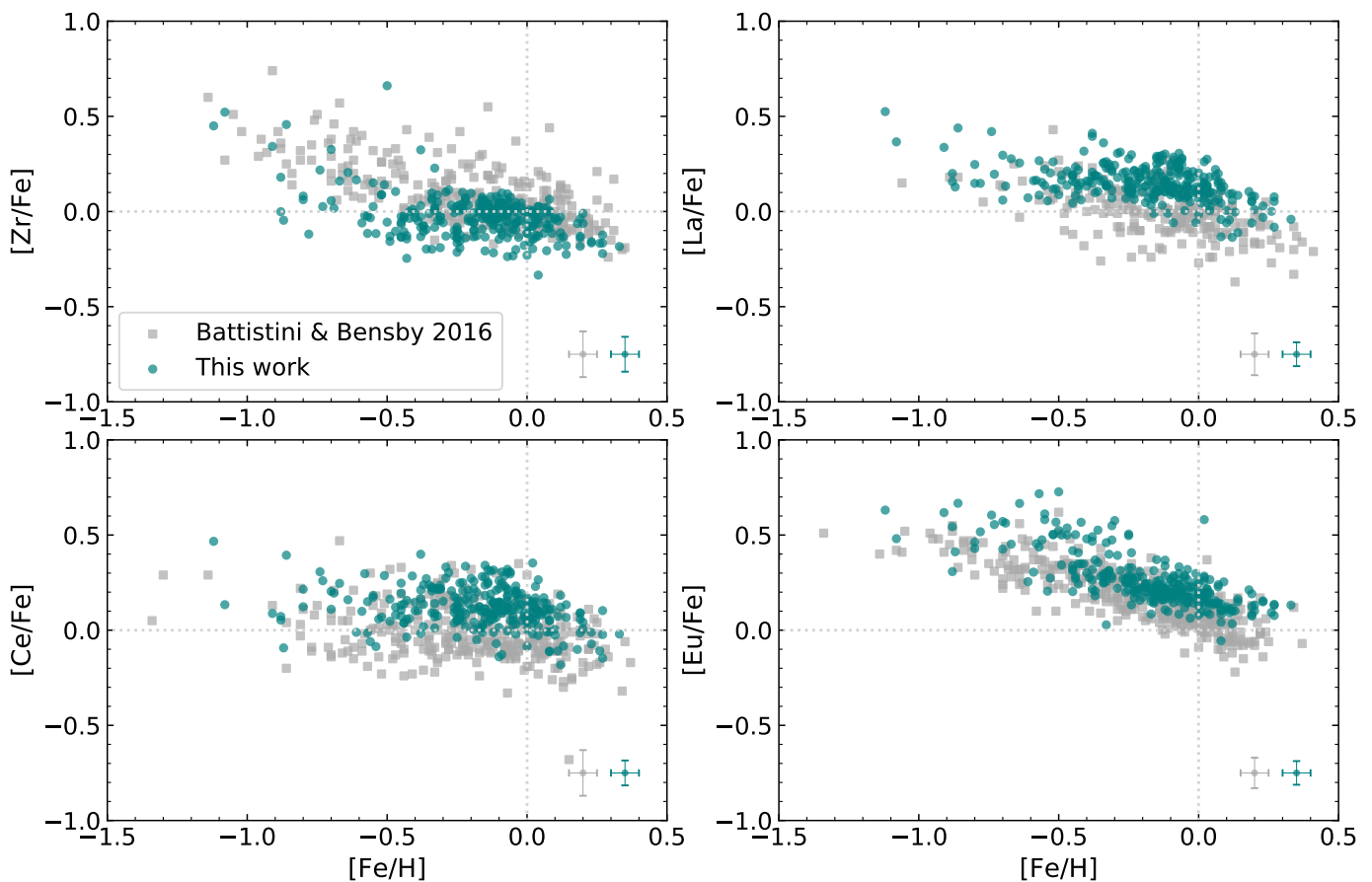


Fig. 4. The determined disk abundances in this work (teal) compared with the determined abundances from Battistini & Bensby (2016) (grey). The typical uncertainty for both data sets is indicated in the lower right corner of every plot, where the uncertainties are taken from Table 6 in Battistini & Bensby (2016).

of the other studies, including ours. Both Johnson et al. (2012) and Van der Swaelmen et al. (2016) produce decreasing $[La/Fe]$ abundances with increasing metallicities, whilst both ours and Duong et al. (2019) exhibit only a very small decrease of $[La/Fe]$ with increasing $[Fe/H]$. In general our $[La/Fe]$ abundances are higher than the other studies, which possibly could point at a higher s-process production in the bulge, compared to previous work. However, we note that our bulge abundances are expected to, similarly as the disk abundances, suffer from a systematic offset in the determined $[La/Fe]$ abundance ratios, preventing us from making a firm claim.

Cerium: Our $[Ce/Fe]$ trend is flat throughout our metallicity range. Duong et al. (2019) also find a flat trend at solar scaled values, but with a slight step-wise increase at $[Fe/H] \sim -0.3$, thereafter following our trend. Van der Swaelmen et al. (2016) find a different $[Ce/Fe]$ trend with decreasing $[Ce/Fe]$ values with increasing metallicities.

Europium: All the published $[Eu/Fe]$ bulge trends and ours decrease with increasing metallicity, although with slightly different slopes and different offsets. The Johnson et al. (2012) study ranges to the lowest metallicities of all the samples. The trend of Duong et al. (2019) and ours trace each other closely with super-solar abundances at all metallicities. The Johnson et al. (2012) and Van der Swaelmen et al. (2016) trends follow each other well, in their overlapping metallicity region, with subsolar abundances above solar metallicities. There is an observable ‘knee’ in the trend around $[Fe/H] \sim -0.4$, seen in all four works. Similarly as $[La/Fe]$, our $[Eu/Fe]$ abundances are

higher than previous works, although due to the possible systematic offsets we cannot draw any firm conclusions from this. However, since the main purpose of this work is to make a differential analysis between the disk and bulge abundances in this work, the possible systematic offset in our analysis is of less importance.

5.2. Disk and bulge comparison of the current study

In this section we compare our abundance-ratio trends, i.e. $[X/Fe]$, for the bulge, the thin, and thick disks as a function of the metallicity for the s-process elements Zr, La, and Ce, and the r-process element Eu. In Fig. 7 we directly compare the bulge population trends with those of the thin and the thick disk populations, determined in the same way in the present study.

The bulge and the disks have very similarly shaped s-process element trends (Zr, La, Ce). The bulge trend of $[La/Fe]$ have a slightly higher overall trend, especially at subsolar metallicities where $[La/Fe]$ is ~ 0.1 dex higher than for the disk. We note that this is the opposite to findings in Duong et al. (2019). The metallicities of the bulge sample extends to slightly higher metallicities, pointing at a higher star formation rate of the bulge. Additionally, Matteucci et al. (2019) shows that implementing a Salpeter like initial mass function (IMF), which favours massive stars compared to typical IMFs for the disk, better reproduce bulge abundances.

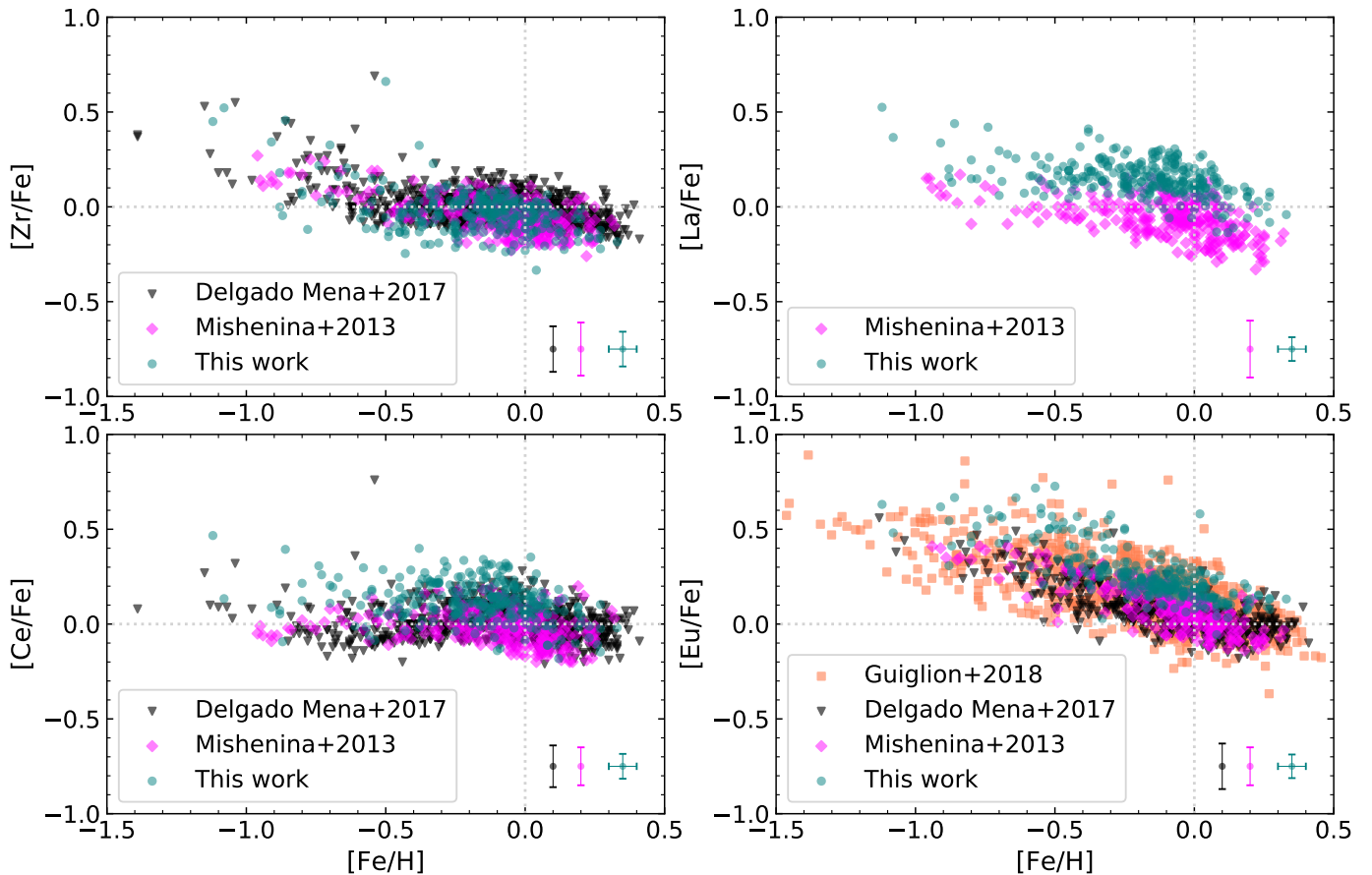


Fig. 5. The determined disk abundances in this work (teal) compared with selected literature trends: Mishenina et al. (2013) (pink), Delgado Mena et al. (2017) (black) and Guiglion et al. (2018) (orange). The typical uncertainty, when available, are indicated in the lower right corner of every plot, where the uncertainties from in Mishenina et al. (2013) and Delgado Mena et al. (2017) (their Table 3 and Table 4, respectively) are for a low T_{eff} star.

For $[\text{Eu}/\text{Fe}]$, the thick disk is enhanced as compared with the thin disk, reminding us of an α -element. The decreasing trend for metallicities larger than $[\text{Fe}/\text{H}] \gtrsim -0.4$ is a result of iron production by SN Ia after a time delay of roughly 100 Myr - 1 Gyr (Matteucci & Brocato 1990; Ballero et al. 2007). The bulge traces the thick disk in the $[\text{Eu}/\text{Fe}]$ abundance, pointing at the bulge having similar star formation rate as that of the thick disk. A plateau, or a knee, can be seen around metallicities of ~ -0.4 for both the thick disk and the bulge. A knee at higher metallicities than in the solar vicinity was already predicted for the bulge by Matteucci & Brocato (1990) and in general for systems with higher star formation rate than in the solar vicinity.

In Fig. 8 we compare Eu with the well-determined α -element magnesium (Mg) (from Jönsson et al. 2017b), by plotting $[\text{Eu}/\text{Mg}]$, for the same stars. The resulting, mostly flat, trend of all populations is already expected from the $[\text{Eu}/\text{Fe}]$ trend, pointing at Eu having a contribution from progenitors of similar timescales as that of progenitors producing Mg (i.e. SNe II). It has indeed been shown by Travaglio et al. (1999) that SNe II progenitors with masses of 8-10 M_{\odot} best reproduce the r-process enrichment in the Galaxy, and Cescutti et al. (2006) showed that to reproduce the ratio of typical s-process elements, such as $[\text{Ba}/\text{Fe}]$, at low metallicities, a r-process production of these elements in stars with masses ranging from 8 to 30 M_{\odot} should be assumed. Nonetheless, the origin of r-elements is, as mentioned earlier, still debated (see e.g. Sneden et al. 2000; Thielemann

et al. 2011; Côté et al. 2019; Siegel et al. 2019; Kajino et al. 2019).

A way to disentangle the s- and r-process contribution throughout the evolution of the Galaxy is to compare an s-process dominated element with that of an r-process dominated one. We thus compare La, with an s-process contribution of 76 %, to that of Eu with an r-process contribution of 94 % (Bisterzo et al. 2014), plotted as $[\text{La}/\text{Eu}]$ in Fig. 9. A pure r-process line is added, using the values from (Bisterzo et al. 2014). The value of the pure r-process line is calculated by subtracting the predicted s-process abundance from the Solar System total values, i.e by treating the r-process as a residual (Bisterzo et al. 2014).

The trends in Fig. 9 show that the r-process dominates more and more the production of neutron-capture elements when the metallicity decreases, reaching $[\text{La}/\text{Eu}] = -0.25$ for the bulge and $[\text{La}/\text{Eu}] = -0.4$ for the thick disk at $[\text{Fe}/\text{H}] \sim -0.5$. With regard to the large scatter at supersolar metallicities, we refrain any further interpretations of the bulge abundances at these metallicities. At around $[\text{Fe}/\text{H}] \sim -0.6$ the $[\text{La}/\text{Eu}]$ thick disk trend levels off or even increases with lower metallicities. Whether this is significant or not is yet to be answered and observations of more stars in this metallicity range are needed. The in general higher $[\text{La}/\text{Eu}]$ abundances of the bulge compared with those of the thick disk point at the bulge having either less r-process production (in turn, possibly a different amount of SNe II), or a

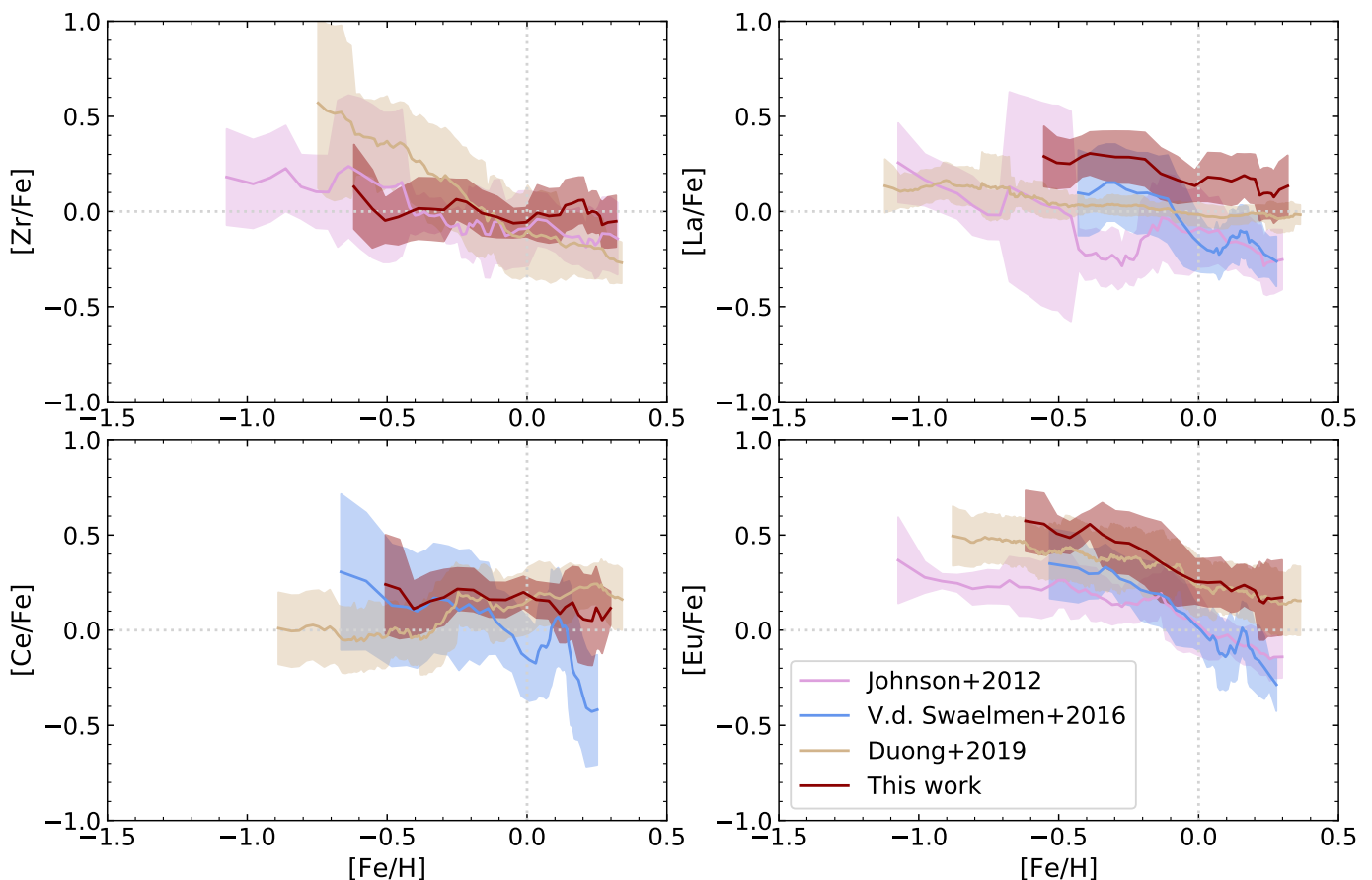


Fig. 6. The running mean for the bulge abundances determined in this work (red solid line) compared with the calculated running mean based on the abundances in Johnson et al. (2012) (pink solid line), Van der Swaelmen et al. (2016) (blue solid line) and Duong et al. (2019) (beige solid line), with a 1σ scatter (shaded regions, same colours as solid lines).

higher s-process contribution (as seen previously in the $[\text{La}/\text{Fe}]$ -trend) than that of the thick disk.

5.3. First- and second-peak s-process elements

In Fig. 10, the running mean of the ratio of the second-peak s-process elements (a mean of La and Ce) and the first-peak s-process element Zr are plotted against metallicity. The trend, elaborated on in the last paragraph of this section, can be explained by considering the stellar yields from Karakas & Lugaro (2016), where low-mass AGB stars have a higher relative production of second-peak elements compared to the production of first-peak element.

The neutrons in the s-process come from two neutron sources, the $^{13}\text{C}(\alpha, n)^{16}\text{O}$ - and the $^{22}\text{Ne}(\alpha, n)^{25}\text{Mg}$ -reaction. The ^{13}C source has a lower neutron density of roughly 10^7 neutrons/cm³, whereas the neutron density for the ^{22}Ne source is around 10^{15} neutrons/cm³. However, due to the longer timescales of the ^{13}C reaction ($\sim 10^3$ years compared to ~ 10 years), the time integrated neutron flux for this neutron source is much higher than for the ^{22}Ne source. Due to this, the ^{13}C reaction builds up the heavier s-process elements, such as the second- (and third-) peak elements, whilst the ^{22}Ne reaction is limited to producing the first-peak s-process elements (Karakas & Lattanzio 2014).

Furthermore, Bisterzo et al. (2017) elaborate on the importance of the size of the ^{13}C -pocket in the s-process production.

The ^{22}Ne reaction takes place only in initially more massive (AGB) stars of $> 4 M_{\odot}$, due to the higher temperatures of these stars (Karakas & Lattanzio 2014). This shrinks the ^{13}C -pocket, resulting in a smaller quantity of s-elements to be expected, *especially* the heavier ones. In short: heavier AGB stars produce relatively fewer second-peak elements compared to low-mass AGB stars, and the latter have a longer time delay.

Another aspect to keep in mind is that at lower metallicities, the number of neutrons to the number of available ^{56}Fe -seeds is higher, compared to higher metallicities, which enables the build-up of second-peak elements (Busso et al. 1999).

In Fig. 10 we first see an increasing trend in the thick disk for increasing metallicities, which turns over for solar metallicities and higher. Below solar metallicities (and above $[\text{Fe}/\text{H}] \sim -0.5$), all trends show an enrichment of second-peak as compared to first-peak elements. This is therefore explained by the low-mass AGB stars which has not yet enriched the interstellar medium (ISM) at the time of the formation of the older thick disk stars, resulting in relatively low $[(\text{La}+\text{Ce})/\text{Zr}]$ abundances at early times.

At solar metallicities, the disk populations does not show any clear differences. As for the bulge, it follows the trend of the thick disk more closely than that of the thin disk, at subsolar metallicities. At supersolar metallicities, the first-peak elements seem to increase in the bulge, possibly explained by a contribution of metal-rich AGB stars, producing a higher amount of first-peak elements (Karakas & Lugaro 2016).

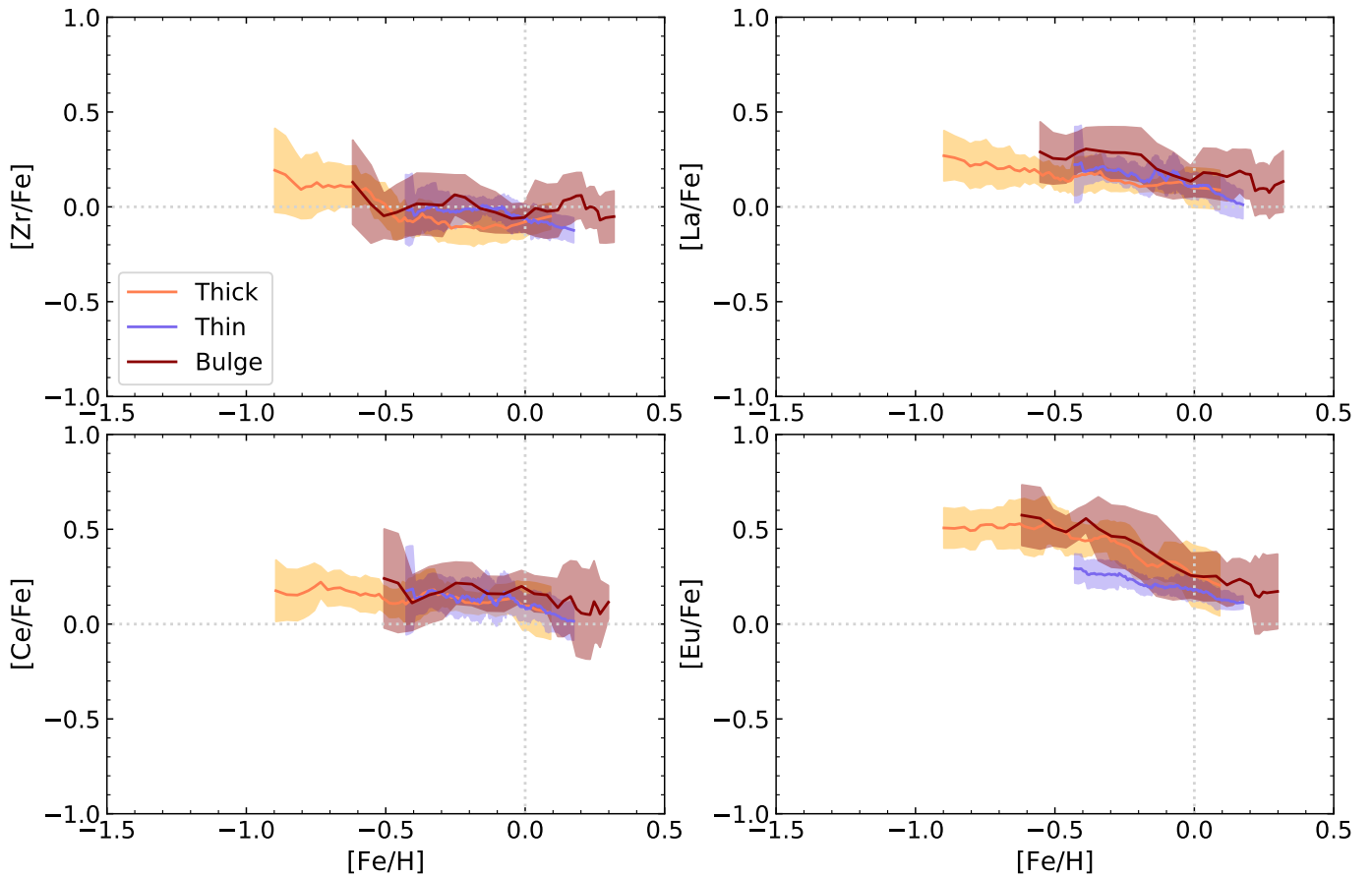


Fig. 7. The running mean for the bulge (red solid line) compared with running mean of the thick disk (yellow solid line) and thin disk (blue solid line), with a 1σ scatter (shaded regions, same colours as solid lines).

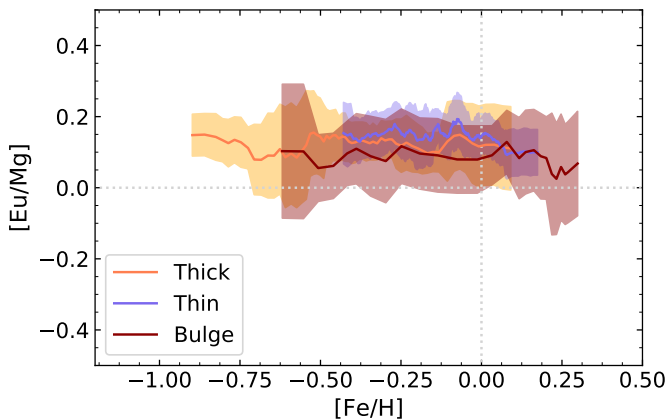


Fig. 8. [Eu/Mg] abundances against [Fe/H] as running mean with a 1σ scatter for the thin disk (blue), thick disk (yellow) and bulge (red).

6. Conclusions

In this work we have determined abundances of the neutron-capture elements Zr, La, Ce and Eu in 45 bulge giants and 291 local disk giants. The determination has been done using high-resolution spectra obtained with FLAMES/UVES (bulge sample) or either FIES or PolarBase (disk sample) and the analysis code SME.

All spectra are evaluated over the wavelength region 5800 - 6800 Å and the careful, manual, definition of the continuum

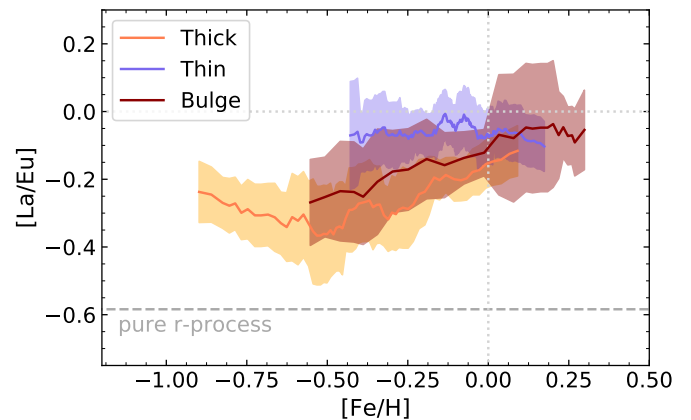


Fig. 9. [La/Eu] abundances against [Fe/H] as running mean with a 1σ scatter for the thin disk (blue), thick disk (yellow) and bulge (red). A pure r-process line is plotted, calculated using the values presented in Bisterzo et al. (2014)

surrounding the spectral lines of interest in the spectra have been crucial in order to get high-precision abundances. Synthetic spectra allows the modelling and handling of blends in the spectra, as well as accounting for hyperfine splitting (in the cases of La, Eu). Isotopic shifts has also been taken into account by manually scaling the $\log(gf)$ -values of the identified transitions in the line list (for the isotopes of Zr, Ce, Eu).

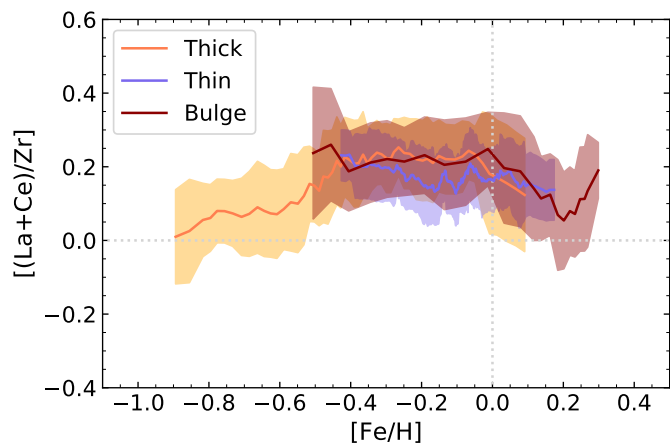


Fig. 10. The abundances ratio of the second-peak s-process elements (La, Ce) and the first-peak s-process element (Zr) against $[Fe/H]$ as running mean with a 1σ scatter for the thin disk (blue), thick disk (yellow) and bulge (red).

The stellar mass and metallicity are factors that contribute to, and affect, the s- and r-process production. Due to this, the enrichment of the ISM and the abundance of neutron-capture elements vary with time in the Galaxy, making them suitable probes for the Galactic chemical evolution.

Our $[Zr, La, Ce/Fe]$ bulge trends are in general flatter than those reported by previous studies, many of which are decreasing with higher metallicities. Such decreasing trends would suggest a higher r-process contribution to these elements in the bulge, while our flatter trends that have the same general shapes as our thick disk trends suggest more similar r/s-proportions in the creation of the neutron capture elements in the bulge and disks. The $[La/Fe]$ bulge trend is ~ 0.1 dex higher compared with the disk, possibly indicating a higher s-process contribution in the bulge, compared with that of the disk.

For $[Eu/Fe]$ we see a decreasing trend with increasing metallicities for both the disk and the bulge, with a plateau at around $[Fe/H] \sim -0.4$. This is very similar to the typical α -element trend, and plotting $[Eu/Mg]$ confirms this, pointing at the r-process having similar production rate as that of Mg (coming from SNe II).

For $[La/Eu]$ we find that towards low metallicities, the abundances lay closer to the pure r-process line (reaching $[La/Eu] -0.4$ (disk) and -0.25 (bulge) at $[Fe/H] \sim -0.5$), indicating that the r-process was the dominating neutron-capture process at early times, both in the disk and the bulge. The results also point at either a) a different amount of massive stars or b) different contribution of the s-process, in the local thick disk and the bulge, where the $[La/Eu]$ abundances seem to be systematically higher in the bulge than that of the thick disk. Since we compare abundances determined with the same method, for stars in the same evolutionary stage, the difference between the disk and the bulge in $[La/Fe]$ could likely be real.

When plotting the ratio of the second- and first-peak s-process elements, $[(La+Ce)/Zr]$, against metallicity we see that the bulge and the thick disk trends follow each other closely. We also show that, according to theoretical predictions by Karakas & Lattanzio (2014), low-mass AGB stars are needed to explain the enhancement of second-peak s-process abundances compared to first-peak s-process abundances.

To conclude, in general, our findings for Zr, Ce, Eu, point at the bulge having similar chemical evolution as that of the local

thick disk, with similar star formation rate. On the other hand, our La trends for the bulge and the thick disk are offset by about 0.1: systematic effects could not be identified in our homogeneous analysis of the bulge and disk samples and further investigation is still required. Our results for the s-process elements differ substantially from previous works, where we find flatter trends. More bulge data would be needed to decrease the scatter and put further constraints on the bulge abundances. Additionally it would be useful to adopt the abundances to Galactic Chemical Evolution models to put further constraints on the evolution of the Galaxy and its components.

Acknowledgements. We would like to thank the referee, Mathieu Van der Swaelmen, for very insightful comments and suggestions that helped to improve this paper in many ways. This research has been partly supported by the Lars Hierta Memorial Foundation, and the Royal Physiographic Society in Lund through Stiftelsen Walter Gyllenbergs fond and Märta och Erik Holmbergs donation. H.J. acknowledges support from the Crafoord Foundation, Stiftelsen Olle Engkvist Byggmästare, and Ruth och Nils-Erik Stenbäcks stiftelse. This work has made use of data from the European Space Agency (ESA) mission *Gaia* (<https://www.cosmos.esa.int/gaia>), processed by the *Gaia* Data Processing and Analysis Consortium (DPAC, <https://www.cosmos.esa.int/web/gaia/dpac/consortium>). Funding for the DPAC has been provided by national institutions, in particular the institutions participating in the *Gaia* Multilateral Agreement. This publication made use of the SIMBAD database, operated at CDS, Strasbourg, France; NASA's Astrophysics Data System; and the VALD database, operated at Uppsala University, the Institute of Astronomy RAS in Moscow, and the University of Vienna.

References

- Abbott, B. P., Abbott, R., Abbott, T. D., et al. 2017, *Phys. Rev. Lett.*, 119, 161101
- Bailer-Jones, C. A. L., Rybizki, J., Fouvras, M., Mantelet, G., & Andrae, R. 2018, *AJ*, 156, 58
- Ballerio, S. K., Matteucci, F., Origlia, L., & Rich, R. M. 2007, *A&A*, 467, 123
- Barbuy, B., Chiappini, C., & Gerhard, O. 2018, *ARA&A*, 56, 223
- Battistini, C. & Bensby, T. 2016, *A&A*, 586, A49
- Bensby, T., Feltzing, S., & Oey, M. S. 2014, *A&A*, 562, A71
- Biemont, E., Grevesse, N., Hannaford, P., & Lowe, R. M. 1981, *ApJ*, 248, 867, (BGHL)
- Bisterzo, S., Travaglio, C., Gallino, R., Wiescher, M., & Käppeler, F. 2014, *ApJ*, 787, 10
- Bisterzo, S., Travaglio, C., Wiescher, M., Käppeler, F., & Gallino, R. 2017, *ApJ*, 835, 97
- Brooke, J. S. A., Bernath, P. F., Schmidt, T. W., & Bacskaý, G. B. 2013, *J. Quant. Spec. Radiat. Transf.*, 124, 11
- Buder, S., Asplund, M., Duong, L., et al. 2018, *MNRAS*, 478, 4513
- Burbidge, E. M., Burbidge, G. R., Fowler, W. A., & Hoyle, F. 1957, *Reviews of Modern Physics*, 29, 547
- Busso, M., Gallino, R., & Wasserburg, G. J. 1999, *Annual Review of Astronomy and Astrophysics*, 37, 239
- Cardelli, J. A., Clayton, G. C., & Mathis, J. S. 1989, *ApJ*, 345, 245
- Cescutti, G., François, P., Matteucci, F., Cayrel, R., & Spite, M. 2006, *A&A*, 448, 557
- Chang, T. L., Qian, Q.-Y., Zhao, M.-T., & Wang, J. 1994, *International Journal of Mass Spectrometry and Ion Processes*, 139, 95
- Chang, T.-L., Qian, Q.-Y., Zhao, M.-T., Wang, J., & Lang, Q.-Y. 1995, *International Journal of Mass Spectrometry and Ion Processes*, 142, 125
- Côté, B., Eichler, M., Arcones, A., et al. 2019, *ApJ*, 875, 106
- Couch, R. G., Schmiedekamp, A. B., & Arnett, W. D. 1974, *ApJ*, 190, 95
- Cristallo, S., Abia, C., Straniero, O., & Piersanti, L. 2015, *ApJ*, 801, 53
- de Laeter, J. R. & Bukilic, N. 2005, *International Journal of Mass Spectrometry*, 244, 91
- Delgado Mena, E., Tsantaki, M., Adibekyan, V. Z., et al. 2017, *A&A*, 606, A94
- Duong, L., Asplund, M., Nataf, D. M., Freeman, K. C., & Ness, M. 2019, *MNRAS*, 486, 5349
- Gaia Collaboration, Brown, A. G. A., Vallenari, A., et al. 2018, *A&A*, 616, A1
- Gaia Collaboration, Prusti, T., de Bruijne, J. H. J., et al. 2016, *A&A*, 595, A1
- Gonzalez, O. A., Rejkuba, M., Zoccali, M., et al. 2011, *A&A*, 530, A54
- Gonzalez, O. A., Rejkuba, M., Zoccali, M., et al. 2012, *A&A*, 543, A13
- Gonzalez, O. A., Zoccali, M., Vasquez, S., et al. 2015, *A&A*, 584, A46
- Grevesse, N., Asplund, M., & Sauval, A. J. 2007, *Space Sci. Rev.*, 130, 105
- Grevesse, N., Scott, P., Asplund, M., & Sauval, A. J. 2015, *A&A*, 573, A27
- Gruyters, P., Lind, K., Richard, O., et al. 2016, *A&A*, 589, A61

Guiglion, G., de Laverny, P., Recio-Blanco, A., & Prantzos, N. 2018, *A&A*, 619, A143

Gustafsson, B., Edvardsson, B., Eriksson, K., et al. 2008, *A&A*, 486, 951

Hayden, M. R., Bovy, J., Holtzman, J. A., et al. 2015, *ApJ*, 808, 132

Heiter, U., Lind, K., Asplund, M., et al. 2015, *Phys. Scr.*, 90, 054010

Herwig, F. 2005, *ARA&A*, 43, 435

Hinkle, K., Wallace, L., Harmer, D., Ayres, T., & Valenti, J. 2000, in *IAU Joint Discussion*, Vol. 24, 26

Immeli, A., Samland, M., Gerhard, O., & Westera, P. 2004, *A&A*, 413, 547

Jofré, P., Heiter, U., Soubiran, C., et al. 2015, *A&A*, 582, A81

Johnson, C. I., Rich, R. M., Kobayashi, C., & Fulbright, J. P. 2012, *ApJ*, 749, 175

Jönsson, H., Ryde, N., Nordlander, T., et al. 2017a, *A&A*, 598, A100

Jönsson, H., Ryde, N., Schultheis, M., & Zoccali, M. 2017b, *A&A*, 600, C2

Kajino, T., Aoki, W., Balantekin, A. B., et al. 2019, *Progress in Particle and Nuclear Physics*, 107, 109

Karakas, A. I. & Lattanzio, J. C. 2014, *PASA*, 31, e030

Karakas, A. I. & Lugaro, M. 2016, *ApJ*, 825, 26

Korn, A. J., Grundahl, F., Richard, O., et al. 2007, *ApJ*, 671, 402

Kratz, K.-L., Farouqi, K., Pfeiffer, B., et al. 2007, *ApJ*, 662, 39

Lawler, J. E., Bonvallet, G., & Sneden, C. 2001a, *Astrophys. J.*, 556, 452, (LBS)

Lawler, J. E., Sneden, C., Cowan, J. J., Ivans, I. I., & Den Hartog, E. A. 2009, *Astrophys. J. Suppl. Ser.*, 182, 51, (LSCI)

Lawler, J. E., Wickliffe, M. E., den Hartog, E. A., & Sneden, C. 2001b, *Astrophys. J.*, 563, 1075, (LWHS)

Lecureur, A., Hill, V., Zoccali, M., et al. 2007, *A&A*, 465, 799

Lind, K., Bergemann, M., & Asplund, M. 2012, *MNRAS*, 427, 50

Lind, K., Korn, A. J., Barklem, P. S., & Grundahl, F. 2008, *A&A*, 490, 777

Liu, F., Asplund, M., Yong, D., et al. 2019, *A&A*, 627, A117

Lomaeva, M., Jönsson, H., Ryde, N., Schultheis, M., & Thorsbro, B. 2019, *A&A*, 625, A141

Marquardt, D. W. 1963, *Journal of the society for Industrial and Applied Mathematics*, 11, 431

Mashonkina, L. & Gehren, T. 2000, *A&A*, 364, 249

Matteucci, F. & Brocato, E. 1990, *ApJ*, 365, 539

Matteucci, F., Grisoni, V., Spitoni, E., et al. 2019, *MNRAS*, 487, 5363

McMillan, P. J. 2018, *Research Notes of the American Astronomical Society*, 2, 51

McWilliam, A. 2016, *Publications of the Astronomical Society of Australia*, 33, e040

Meléndez, J., Asplund, M., Alves-Brito, A., et al. 2008, *A&A*, 484, L21

Mishenina, T. V., Pignatari, M., Korotin, S. A., et al. 2013, *A&A*, 552, A128

Nomura, M., Kogure, K., & Okamoto, M. 1983, *International Journal of Mass Spectrometry and Ion Processes*, 50, 219

Nordlander, T., Korn, A. J., Richard, O., & Lind, K. 2012, *ApJ*, 753, 48

Pedregosa, F., Varoquaux, G., Gramfort, A., et al. 2011, *Journal of machine learning research*, 12, 2825

Petit, P., Louge, T., Théado, S., et al. 2014, *PASP*, 126, 469

Piskunov, N. & Valenti, J. A. 2017, *A&A*, 597, A16

Portail, M., Gerhard, O., Wegg, C., & Ness, M. 2017, *MNRAS*, 465, 1621

Prochaska, J. X. & McWilliam, A. 2000, *ApJ*, 537, L57

Shen, J. & Li, Z.-Y. 2016, in *ASSL*, Vol. 418, *Galactic Bulges*, ed. E. Laurikainen, R. Peletier, & D. Gadotti, 233

Siegel, D. M., Barnes, J., & Metzger, B. D. 2019, *Nature*, 569, 241

Sneden, C., Cowan, J. J., Ivans, I. I., et al. 2000, *The Astrophysical Journal Letters*, 533, L139

Sneden, C., Lucatello, S., Ram, R. S., Brooke, J. S. A., & Bernath, P. 2014, *ApJS*, 214, 26

Souto, D., Allende Prieto, C., Cunha, K., et al. 2019, *ApJ*, 874, 97

Telting, J. H., Avila, G., Buchhave, L., et al. 2014, *Astronomische Nachrichten*, 335, 41

Thielemann, F.-K., Arcones, A., Käppeli, R., et al. 2011, *Progress in Particle and Nuclear Physics*, 66, 346, *particle and Nuclear Astrophysics*

Thielemann, F. K., Eichler, M., Panov, I. V., & Wehmeyer, B. 2017, *Annual Review of Nuclear and Particle Science*, 67, 253

Thielemann, F.-K., Isern, J., Perego, A., & von Ballmoos, P. 2018, *Space Sci. Rev.*, 214, 62

Thorsbro, B., Ryde, N., Schultheis, M., et al. 2018, *ApJ*, 866, 52

Thygesen, A. O., Frandsen, S., Bruntt, H., et al. 2012, *A&A*, 543, A160

Travaglio, C., Galli, D., Gallino, R., et al. 1999, *ApJ*, 521, 691

Travaglio, C., Gallino, R., Arnone, E., et al. 2004, *ApJ*, 601, 864

Valenti, J. A. & Piskunov, N. 1996, *A&AS*, 118, 595

Van der Swaelmen, M., Barbay, B., Hill, V., et al. 2016, *A&A*, 586, A1

Velichko, A. B., Mashonkina, L. I., & Nilsson, H. 2010, *Astronomy Letters*, 36, 664

Wegg, C., Gerhard, O., & Portail, M. 2015, *MNRAS*, 450, 4050

Weiland, J. L., Arendt, R. G., Berriman, G. B., et al. 1994, *ApJ*, 425, L81

Zasowski, G., Schultheis, M., Hasselquist, S., et al. 2019, *ApJ*, 870, 138

Table A.1. Basic data for the observed bulge giants. The S/N per data point is measured by the IDL-routine `der_snr.pro`, see http://www.stecf.org/software/ASTROsoft/DER_SNR.

Star ^a	RA (J2000) (h:m:s)	Dec (J2000) (d:am:as)	V	S/N
SW-09	17:59:04.533	-29:10:36.53	16.153	16
SW-15	17:59:04.753	-29:12:14.77	16.326	15
SW-17	17:59:08.138	-29:11:20.10	16.388	11
SW-18	17:59:06.455	-29:10:30.53	16.410	14
SW-27	17:59:04.457	-29:10:20.67	16.484	13
SW-28	17:59:07.005	-29:13:11.35	16.485	16
SW-33	17:59:03.331	-29:10:25.60	16.549	14
SW-34	17:58:54.418	-29:11:19.82	16.559	12
SW-43	17:59:04.059	-29:13:30.26	16.606	16
SW-71	17:58:58.257	-29:12:56.97	16.892	14

Notes. This is only an excerpt of the table to show its form and content. The complete table is available in electronic form at the CDS.

^a Using the same naming convention as Lecureur et al. (2007) for the B3-BW-B6-BL-stars.

Appendix A: Additional tables

Table A.2. Basic data for the observed solar neighbourhood giants. Coordinates and magnitudes are taken from the SIMBAD database, while the radial velocities are measured from the spectra. The S/N per data point is measured by the IDL-routine `der_snr.pro`, see http://www.stecf.org/software/ASTROsoft/DER_SNR.

HIP/KIC/TYC	Alternative name	RA (J2000) (h:m:s)	Dec (J2000) (d:am:as)	V	v_{rad} km/s	S/N	Source
HIP1692	HD1690	00:21:13.32713	-08:16:52.1625	9.18	18.37	114	FIES-archive
HIP9884	alfAri	02:07:10.40570	+23:27:44.7032	2.01	-14.29	90	PolarBase
HIP10085	HD13189	02:09:40.17260	+32:18:59.1649	7.56	26.21	156	FIES-archive
HIP12247	81Cet	02:37:41.80105	-03:23:46.2201	5.66	9.34	176	FIES-archive
HIP28417	HD40460	06:00:06.03883	+27:16:19.8614	6.62	100.64	121	PolarBase
HIP33827	HR2581	07:01:21.41827	+70:48:29.8674	5.69	-17.99	79	PolarBase
HIP35759	HD57470	07:22:33.85798	+29:49:27.6626	7.67	-30.19	85	PolarBase
HIP37447	alfMon	07:41:14.83257	-09:33:04.0711	3.93	11.83	71	Thygesen et al. (2012)
HIP37826	betGem	07:45:18.94987	+28:01:34.3160	1.14	3.83	90	PolarBase
HIP43813	zetHya	08:55:23.62614	+05:56:44.0354	3.10	23.37	147	PolarBase

Notes. This is only an excerpt of the table to show its form and content. The complete table is available in electronic form at the CDS.

Table A.3. Stellar parameters and determined abundances for observed bulge giants. [Fe/H] is listed in the scale of Grevesse et al. (2015).

Star	T_{eff}	$\log g$	[Fe/H]	v_{micro}	A(Zr)	A(La)	A(Ce)	A(Eu)
SW-09	4095	1.79	-0.15	1.32	2.79	1.09	1.72	0.75
SW-15	4741	1.96	-0.98	1.62	1.51	...
SW-17	4245	2.09	0.24	1.44	2.95	1.26	...	0.97
SW-18	4212	1.67	-0.13	1.49	2.30	0.84	1.86	0.86
SW-27	4423	2.34	0.11	1.60	2.73	1.22	2.09	1.05
SW-28	4254	2.36	-0.14	1.44	2.26	1.42	2.45	0.91
SW-33	4580	2.72	0.16	1.39	2.55	1.60	2.29	1.05
SW-34	4468	1.75	-0.45	1.63	2.34	1.04
SW-43	4892	2.34	-0.77	1.84	...	0.75	...	0.28
SW-71	4344	2.66	0.39	1.31	3.10	1.77

Notes. This is only an excerpt of the table to show its form and content. The complete table is available in electronic form at the CDS.

Table A.4. Stellar parameters and determined abundances for observed solar neighbourhood giants. [Fe/H] is listed in the scale of Grevesse et al. (2015).

HIP/KIC/TYC	T_{eff}	$\log g$	[Fe/H]	v_{micro}	A(Zr)	A(La)	A(Ce)	A(Eu)
HIP1692	4216	1.79	-0.26	1.55	2.20	0.97	1.41	0.51
HIP9884	4464	2.27	-0.21	1.34	2.34	1.08	1.55	0.53
HIP10085	4062	1.44	-0.32	1.63	2.32	1.03	1.48	0.51
HIP12247	4790	2.71	-0.04	1.40	2.57	1.28	1.74	0.63
HIP28417	4746	2.56	-0.25	1.40	2.24	1.02	1.39	0.52
HIP33827	4235	1.99	0.01	1.50	2.61	1.23	1.68	0.72
HIP35759	4606	2.47	-0.15	1.42	2.23	1.06	1.54	0.74
HIP37447	4758	2.73	-0.04	1.35	2.49	1.26	1.75	0.71
HIP37826	4835	2.93	0.07	1.24	2.68	1.33	1.79	0.73
HIP43813	4873	2.62	-0.07	1.51	2.61	1.35	1.83	0.63

Notes. This is only an excerpt of the table to show its form and content. The complete table is available in electronic form at the CDS.